Control of the Flexural Axis of a Wing with Piezoelectric Actuation

James Davis*
U.S. Air Force Research Laboratory, Eglin Air Force Base, Florida 32542
and
Nam H. Kim[†] and Rick Lind[‡]
University of Florida, Gainesville, Florida 32611

Through aeroelastic effects, the various structural parameters of a wing can have significant effects on the flight dynamics of any size of aerial vehicle. If these parameters could be manipulated in flight, the aeroelastic interactions could, in turn, be leveraged for control purposes. If done properly, this approach has the potential to yield a significant improvement over conventional control surfaces for highly aeroelastic vehicles in terms of maneuverability. In this paper, the preliminary analysis of a proposed structural system with this capability is presented. The proposed system is a combination of a highly flexible conventionally configured wing structure, piezoelectric actuation, and a feedback loop. This system embeds a haptic system into the rear spar of the wing, the effects of which are adjustable by means of a gain parameter. The analysis presented in this paper shows the feasibility of the design and effectiveness of an unoptimized configuration, relocating the flexural axis by approximately 22%. This preliminary analysis establishes that the presented structural-parameter-actuation design, termed flexural-axis control, is practical and realizable.

Nomenclature

A	=	area, mm^2
$\mathbf{C}$	=	compliance matrix
C_{ki}^E	=	piezoelectric elastic stiffness constants
c	=	chord length, mm
d_{ij}	=	piezoelectric constants
E	=	modulus of elasticity, GPa
G	=	shear modulus
Gn	=	gain parameter
I	=	area of inertia, mm^4
$\mathbf{K}$	=	stiffness matrix
L	=	element length, mm
Lf	=	applied point load, N
Mo	=	applied point moment, N · m
Rt	=	applied point torque, N · m
w	=	vertical deflection, mm
x_{fa}	=	location of the flexural axis
ϵ	=	strain
θ	=	rotational deflection, deg
κ	=	curvature
Ω_j	=	applied electric field, V/mm

I. Introduction

ONE of the primary objectives in aeroelasticity, as a practical implementation, is the determination of stability limits and defining the boundaries of the flight envelope for the given vehicle configuration. Some researchers have observed that, with the appropriate structural parameters, aeroelastic effects and interactions could be leveraged advantageously in the interior of the flight envelope to mitigate influence from atmospheric disturbances, such as gusts or turbulence [1,2]. It has also been suggested that the ability to manipulate the structural parameters in flight could be used to selectively enhance the maneuvering capability through aeroelastic coupling [3]. These operational concepts of enhanced stability through passive deformation and the manipulation of parameters for maneuverability are complementary, each offering solutions to the others' shortcomings, and not mutually exclusive.

Researchers, primarily focusing on conventional scale aircraft, have investigated the practical issues of implementing the concept of manipulating structural parameters. Kota et al. [4] proposed changing the area moment of inertia for the structures' cross section by disengaging the web of the wing spars. Chen et al. [5] developed the variable-stiffness-spar concept, which consisted of rotating a segmented rectangular spar connected to the wing ribs by articulated joints. To vary the torsional stiffness of the wing, the spar was rotated through 90 deg with an electrical actuator. Amprikidis and Cooper [6] implemented a three-spar wing box, wherein the intermediate spar was translated in the chordwise direction. Cooper [7] discusses the analysis results for both translating and rotating spar concepts, both of which vary the torsional and bending stiffness, and the shear-center position with the objective of minimizing drag while maintaining lift. While the designs proposed in these reports are theoretically sound, they illustrate that the conventional aircraft structural configuration of a built-up semimonocoque design does not readily lend itself to manipulation due to high stiffness and complicated interdependencies. The reader is referred to Barbarino et al. [8] for a thorough review of morphing designs and accomplishments, in which the design proposed here would be in the category of twist using active aeroelastic concepts.

It is generally accepted that the flexibility of a wing structure tends to hinder maneuvering performance. Maneuverability, being dependent on wing loading and inherent, or passive, stability, requires motions and deformations to be in a decremental direction when prompted by an increase in loading, thereby limiting the maximum attainable. Conventionally, to maximize maneuverability, advanced control schemes are leveraged to allow smaller inherent stability margins or even inherent instability, there in maximizing the availability of wing loading. Unfortunately, these advanced control schemes typically are more expensive and difficult to develop, which act as a disincentive for implementation on lower cost and expendable vehicles. More relevant to the topic of this paper is the low inherent stability margins, or instability tends to make the vehicle

*Research Engineer, Munitions Directorate, Computational Sciences Branch; james.davis.20@us.af.mil. Member AIAA.
[†]Associate Professor, Department of Mechanical and Aerospace Engineering; nkim@ufl.edu. Associate Fellow AIAA.
[‡]Associate Professor, Department of Mechanical and Aerospace Engineering; ricklind@ufl.edu. Associate Fellow AIAA.

more susceptible to atmospheric disturbances, in turn driving further complexity into the control scheme through tighter loops or additional algorithms.

With the objective of manipulating structural parameters, or their effective values, given a limited influential capability it is logical that the lower the initial values the more relative change that could be imparted. Therefore, starting with a design intended to have significant inherent stability through deformations, and implementing a methodology in which a pertinent parameter could be changed whenever desired, dramatic improvements in maneuvering performance could be realized through the aeroelastic coupling of the entire system. Pursuing this concept will enable the optimization of the structural system toward two conditions simultaneously, instead of selecting one over the other to the detriment of both.

The long-term goal of this research is to explore the expanded design space resulting from the union of these concepts and the implications on flight dynamics. In this paper, we show that the design goal is achievable by presenting the preliminary analysis of a structural system that is capable of changing the structural parameters, primarily of which is the location of the flexural axis.

The preliminary analysis will be conducted by first representing the structure mathematically, and then simplifying it through applications of various assumptions. Next, the simplified representation will be used to find the location of the flexural axis x_{fa} in terms of the stiffness parameters of the original members. Finally, an equivalent beam will be formulated at the flexural-axis location, with its bending and twisting stiffness parameters derived in terms of the stiffness parameters of the original members. The behavior of the complete structure in response to applied forces can then be represented by the single equivalent beam at the axis location, instead of the complete complex structure.

The derived relations for the flexural-axis location and equivalent beam form the basis of the actuation concept and analysis. With their dependency on the stiffness parameters of the original members established, it is shown that by changing the stiffness of an original member the axis location and equivalent-beam stiffness are subsequently changed as well. Changing the stiffness of an original member is achieved through embedding a haptic, or force-feedback system, into the member. The design and configuration presented in this paper will be referred to as flexural-axis control (FACt), and it will be shown to be effective, practical, and realizable.

II. Formulation

There are four prominent structural parameters, which determine the aeroelastic response of a wing structure: bending stiffness, twisting stiffness, the location of the flexural axis, and the mass distribution [9–11]. The structural configuration used in this work is similar to that discussed by Bisplinghoff et al. [9] for the development of models for aeroelastic wind-tunnel testing. This configuration provides the ability to adjust the bending and twisting stiffness, as well as the location of the flexural axis relatively independent of one another. The full structure is presented in Fig. 1 with a subsection highlighted in a free-body diagram that will be used for this preliminary analysis.

The members of the representative structure are the leading-edge spar, rib, and trailing-edge spar designated in Fig. 1b as 1, 2, and 3, respectively. The members of the structure were mathematically represented using a symbolic form of the linear Euler–Bernoulli beam finite element; the structure was assembled using standard finite element methodologies via the commercially available software package Mathematica. The essential boundary conditions are applied at the root nodes constraining them to fixed positions in the inertial frame. For the two other nodes, noted as leading edge (LE) and trailing edge (TE), deformations in the spanwise and chordwise directions are restricted, as well as rotations about the vertical axis. Application of these boundary conditions reduces the stiffness-matrix entries to the degrees of freedom of interest, which are those associated with the vertical bending and spanwise twisting of the assembly. The stiffness matrix is then further reduced by enforcing that the twist angles of the fore and aft spars (elements 1 and 3) remain equal through the application of a transformation matrix as with standard finite element practices [12]. The stiffness matrix of the structure resulting from these simplifications is presented as

$$\mathbf{K} = \begin{pmatrix} y_{11} + y_{21} & 2y_{22} & -y_{12} & -y_{21} & 0 \\ 2y_{22} & s_1 + s_3 + 2y_{23} + 2y_{24} & 0 & -2y_{22} & 0 \\ -y_{12} & 0 & s_2 + y_{13} & 0 & -s_2 \\ -y_{21} & -2y_{22} & 0 & y_{21} + y_{31} & -y_{32} \\ 0 & 0 & -s_2 & -y_{32} & s_2 + y_{33} \end{pmatrix}$$

(1)

in which $y_{i1} = 12EI_i/L_i^3$, $y_{i2} = 6EI_i/L_i^2$, $y_{i3} = 4EI_i/L_i$, $y_{i4} = 2EI_i/L_i$, and $s_i = GK_i/L_i$, with i being the element number, and I_i being the area inertia associated with bending in the vertical direction. The corresponding degrees of freedom are $(w_{LE} \quad \theta_{rib} \quad \theta x_{LE} \quad w_{TE} \quad \theta x_{TE})^T$, which are the vertical displacement of the leading-edge node, rotation of the rib about the Y axis, rotation of the leading-edge node about the X axis, vertical displacement of the trailing-edge node, and rotation of the trailing-edge node about the X axis, respectively.

Using the extended shape functions associated with the Euler–Bernoulli beam element, the nodal equivalent forces for an applied
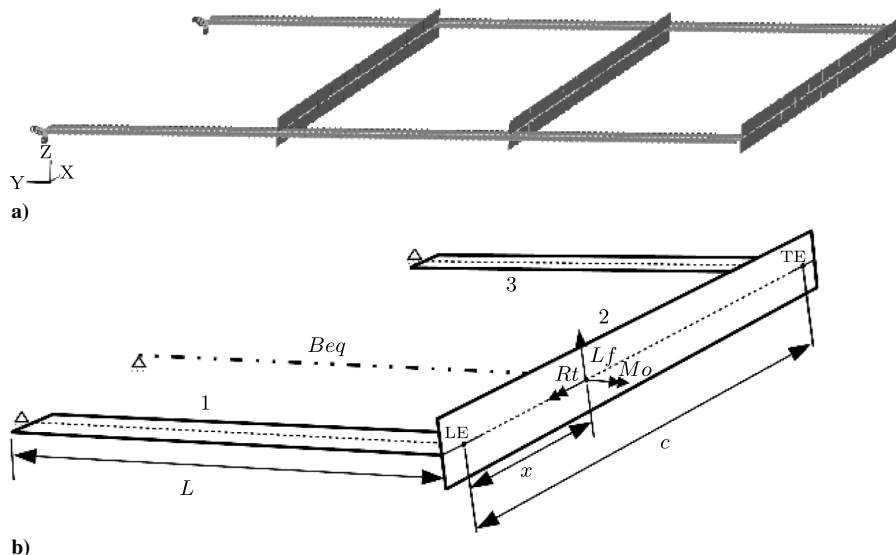

Fig. 1 Structural configuration: a) highly flexible conventionally configured wing structure, and b) representative subsection.

point load Lf at a distance x from the leading edge, after applying the previously mentioned transformation matrix, are

$$\boldsymbol{F}(x) = \left[\begin{array}{ccccc} \frac{Lf(c-x)^2(c+2x)}{c^3} & \frac{Lfx(c^2-3cx+2x^2)}{c^2} & 0 & \frac{Lf(3c-2x)x^2}{c^3} & 0 \end{array} \right]^T \tag{2}$$

Using standard practices and the same shape functions, the equivalent nodal forces due to an applied point moment Mo at a distance x from the leading edge are

$$\boldsymbol{M}(x) = \left(\begin{array}{ccccc} \frac{6Mox(-c+x)}{c^3} & \frac{Mo(c^2-6cx+6x^2)}{c^2} & 0 & \frac{6Mox(c-x)}{c^3} & 0 \end{array} \right)^T \tag{3}$$

And for completeness, the equivalent nodal forces due to an applied point torque Rt along the rib, or element 2, at a distance x from the leading edge are calculated using linear interpolation functions:

$$\boldsymbol{T}(x) = \left(\begin{array}{ccccc} 0 & 0 & \frac{Rt(c-x)}{c} & 0 & \frac{Rtx}{c} \end{array} \right)^T \tag{4}$$

These applied forces, Lf, Mo, and Rt, are shown in Fig. 1b. From the geometry in Fig. 1b, it is observed that the area-moment-of-inertia term I_2, for the rib/element 2, is far greater than that of the spars for bending in the Z direction. This is leveraged for further simplification by assuming that the value of I_2 approaches infinity in the compliance matrix, thus making the rib analytically rigid in the vertical direction, resulting in a reduced compliance matrix:

$$\mathbf{C}_{\text{red}} = \lim_{I_2 \to \infty} \mathbf{K}^{-1} \tag{5}$$

Applying the nodal equivalent forces from the point load to the simplified inverted stiffness matrix gives the relation between the displacements and rotations of the leading- and trailing-edge nodes to the relevant structural properties, as well as the magnitude and location of the various loads applied at the point (x) along element 2 as measured from the leading edge:

$$(w_{LE} \quad \theta_{\text{rib}} \quad \theta x_{LE} \quad w_{TE} \quad \theta x_{TE})^T = \mathbf{C}_{\text{red}} \cdot [\boldsymbol{F}(x) + \boldsymbol{M}(x) + \boldsymbol{T}(x)] \tag{6}$$

III. Flexural Axis

The flexural axis is defined as the location through which an applied vertical force will not cause a rotational displacement of the wing structure about the spanwise axis. The rotational displacement about the spanwise axis, θ_{rib}, as a function of the applied force Lf, the location of application x, and structural properties, is found from Eq. (6) with $Mo = Rt = 0$:

$$\theta_{\text{rib}} = \frac{L^3 Lf (4EI_1 + (1 + E_{\text{ratio}})Ls_2)(-c + x + E_{\text{ratio}}x)}{12c^2 EI_1(EI_1 + (1 + E_{\text{ratio}})Ls_2) + (1 + E_{\text{ratio}})L^3(4EI_1 + (1 + E_{\text{ratio}})Ls_2)(s_2 + s_3)} \tag{7}$$

in which $E_{\text{ratio}} = EI_1/EI_3$.

To find the location of the flexural axis along the rib, Eq. (7) is set equal to zero and solved for x/c. This gives the location of the flexural axis as a function of the structural properties, as a fraction of the chord length

$$x_{\text{fa}} = \frac{x}{c} = \frac{EI_3}{EI_1 + EI_3} \tag{8}$$

This result is identical to what would be obtained with the classic analysis methods for indeterminate structures. The required stiffness ratio as a function of x_{fa} can be found by rearranging Eq. (8), resulting in

$$E_{\text{ratio}} = \frac{EI_1}{EI_3} = \frac{1}{x_{\text{fa}}} - 1 \tag{9}$$

A. Equivalent Beam

To find the compliance matrix of an equivalent-single-beam representation of the structure, Beq as shown in Fig. 1b, the three force vectors previously derived are evaluated as applied at the flexural-axis location, and summed. The sum of the forces is then multiplied into the simplified inverted stiffness matrix, determining the nodal displacements. Then, the calculated nodal displacements are linearly interpolated to the flexural-axis location:

$$\begin{pmatrix} w_{\text{eq}} \\ \theta x_{\text{eq}} \\ \theta y_{\text{eq}} \end{pmatrix} = \begin{pmatrix} (1 - x_{\text{fa}}) & 0 & 0 & x_{\text{fa}} & 0 \\ 0 & 0 & (1 - x_{\text{fa}}) & 0 & x_{\text{fa}} \\ 0 & 1 & 0 & 0 & 0 \end{pmatrix}$$
$$\cdot \mathbf{C}_{\text{red}} \cdot [\boldsymbol{F}(x_{\text{fa}}c) + \boldsymbol{T}(x_{\text{fa}}c) + \boldsymbol{M}(x_{\text{fa}}c)] \tag{10}$$

Finally, the compliance matrix $\mathbf{C}_{\text{eq}}$ for the equivalent single beam Beq is found by factoring out the point loads Lf, Rt, and Mo. This compliance matrix represents two of the four structural parameters, bending stiffness and twisting stiffness, discussed in Sec. II as being significant in the determination of the aeroelastic behavior of the wing:

$$\begin{pmatrix} w_{\text{eq}} \\ \theta x_{\text{eq}} \\ \theta y_{\text{eq}} \end{pmatrix} = \mathbf{C}_{\text{eq}} \begin{pmatrix} Lf \\ Rt \\ Mo \end{pmatrix} \tag{11}$$

Inverting $\mathbf{C}_{\text{eq}}$ gives the stiffness matrix for the equivalent beam $\mathbf{K}_{\text{eq}}$ with fixed-free boundary conditions applied in terms of the torsional stiffness of the members, the bending stiffness of the leading-edge spar, and the location of the flexural axis:

$$\mathbf{K}_{\text{eq}} = \begin{pmatrix} \frac{12(EI_1+EI_3)}{L^3} & -\frac{6(EI_1+EI_3)}{L^2} & 0 \\ -\frac{6(EI_1+EI_3)}{L^2} & \frac{4(EI_1+EI_3)}{L} & 0 \\ 0 & 0 & \frac{L^4 s_2(s_1+s_3)+4LEI_1[3c^2 s_2+L^2(s_1+s_3)]x_{\text{fa}}+12c^2 EI_1^2 x_{\text{fa}}^2}{L^3(Ls_2+4EI_1 x_{\text{fa}})} \end{pmatrix} \tag{12}$$

The established relationships among the structural parameters of axis location and stiffness values form the basis of the manipulation methodology discussed in Sec. IV.

B. Nonlinear Validity

The relations of the flexural-axis location and the equivalent-beam model $\mathbf{K}_{\text{eq}}$ to the stiffness values for the original structure presented previously are based on the linear theory. The validity of extrapolating these relations to a geometrically nonlinear regime was investigated using commercially available finite element software package Abaqus and the structural configuration in Fig. 1b. The range of applied force and moments was selected by increasing the magnitude of the forces until significant geometrically nonlinear deformations were observed. The parameters used for the Abaqus analysis are presented in Table 1.

The axis location estimated from the linearly derived Eq. (8) was evaluated by comparison to nonlinear results extracted from the Abaqus analysis after applying the same load normal to the chord at 12.5, 25, and 50 percent of the chord length. The load applied was a follower type, and as such remained normal to the rib throughout the

deformation reminiscent of an aerodynamic pressure. For each location, the load was applied incrementally by the percentages shown in Table 2 with 100% corresponding to 1.33 N. The resulting rotation about the spanwise axis was taken as a function of the location of the load application, and the zero intercept was found. Values for the zero intercepts are presented in Table 2 for various loading levels and the estimated value from Eq. (8). The results are also presented in Fig. 2, illustrating the process as well as the agreement between the linear and nonlinear formulations.

From the nonlinear analysis, it was also found that the axis location varied less than 0.1% of the chord length over the deflection range investigated.

The equivalent-single-beam compliance matrix in Eq. (12) is based on the linear theory and resulted from condensing the representative structure. Future work will be based on the assertion that the structural system can be represented as a single beam, Beq, placed at the flexural axis. To evaluate the validity of this assertion, an analysis of the representative structure was conducted, again using Abaqus, by applying a vertical force, a chordwise torque, and a spanwise moment to the model at the estimated location of the flexural axis using the stiffness parameters and the estimated axis location shown in Tables 1 and 2. The results of this analysis are presented in Fig. 3, and show a good agreement between the linear estimates and the nonlinear analysis for all three cases of vertical force, chordwise torque, and spanwise moment across the range investigated for the three degrees of freedom.

These results show that the presented method of reducing the structural system to a single equivalent beam, even though based on the linear methods, is valid in the geometrically nonlinear regime. This allows the subsequent analysis to be based on the simplified single equivalent beam instead of the more complicated structural system. The only discrepancy observed that might be of concern is the behavior due to the application of a spanwise moment, in which the nonlinearities result in a twist–bend coupling at moderate deflections. The significance of this discrepancy is application dependent and should be evaluated as part of the implementation process. The purpose of the results presented here is to illustrate the validity and limitations of the linear methodology, and is not intended to be all encompassing or inclusive of the entire range of possible loading conditions in application.

IV.   Axis Control

There have been many past efforts to implement induced-strain actuators for control-effector purposes [13–19], all of which focused on geometric metrics, such as degrees of rotation or distance of deflection. These attempts to exert direct control of vehicle geometry are a key tenant of conventional control or morphing approaches. The design paradigm used to arrive at the presented design is to leverage the significant force-producing capabilities of piezoelectric actuators
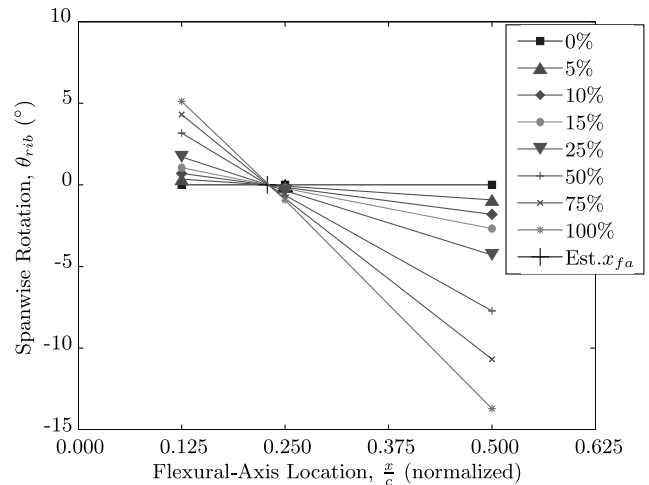
Fig. 2   Results calculated by Abaqus showing the rotation of the rib due to the location of load application and magnitude as a percentage of the maximum, and the estimated location of x_{fa} from Eq. (8).

and define the metric of interest as change in the stiffness properties of the structural system instead of the geometric displacements. This design paradigm is considered in a class of control-system approaches termed *force feedback*; as applied in the presented FACt design, it enables one form of structural-parameter actuation.

The system, in its simplest form, consists of an actuation device configured, such that it attempts to deform a beamlike member, the degree of which is dependent on the deformation of the beam and controlled by the gain term. In control terminology, the system tries to return the beam to a nondeformed configuration, and the gain term influences the rate of response and steady-state error. In application, the physical manifestation of these control terms are realized as, the rate of response is an actuating force per unit deformation, or effective stiffness, and the steady-state error is the resulting deformation.

This structural-parameter-actuation approach of Ehlers and Weisshaar [20,21], Weisshaar [22], and Weisshaar and Ehlers [23], even though they do not explicitly state any design philosophy, is another implementation of this concept. The research presented therein focused on the aeroelastic behavior of a swept wing, and as such the location and direction of the flexural axis are dependent on the torsional stiffness of the wing. From that, the implementation was based on using embedded actuators to apply a distributed torque to the main structure of the swept wing, the actuation magnitude of which was tied to a deformation sensor. Changing the gain of this feedback loop would in turn influence the angle of the flexural axis, sweeping it about a fixed point at the wing root.

For a beamlike device, there are three generally possible degrees of freedom to which actuation could be applied; extension/contraction, bending, and twisting. Each of the three actuating degrees of freedom was considered for utilization on each member of the representative subsection. The design paradigm implemented focuses on affecting the stiffness parameters of a structural system. With that in mind, the simplified structural model presented in Eqs. (8) and (12) can be used to provide insight into which a combination of actuation and member will have the most significant effect.

The bending-stiffness parameters, EI_1 and EI_3, are the only parameters present in all terms of Eqs. (8) and (12). From Eq. (8), it is observed that a positive change in the axis location, moving it further aft, would require either a decrease in the EI_1 term or an increase in the EI_3 term. From the preceding analysis, to decrease the stiffness of a member would require a negative gain. In turn, this inversion would induce an actuation moment in the direction of the deforming force, feeding back into itself, forming a divergent control loop, or requiring the use of a more complex control logic. Increasing the EI_3 term uses the simple feedback loop in a stable manner, and moves the axis location in the desired direction. From this conceptual analysis, it is determined that a bending-type actuator applied to the upper surface of the rear spar would be the most direct and influential over the

Table 1   Values of structural parameters

	Length, mm	Height, mm	Width, mm	I, mm^4	E, GPa
Leading-edge spar	177.8	0.381	12.7	58.534E − 03	148.0
Trailing-edge spar	177.8	0.254	12.7	17.343E − 03	148.0
Rib	152.4	12.7	0.381	65.036	148.0

Table 2   Flexural-axis calculation results

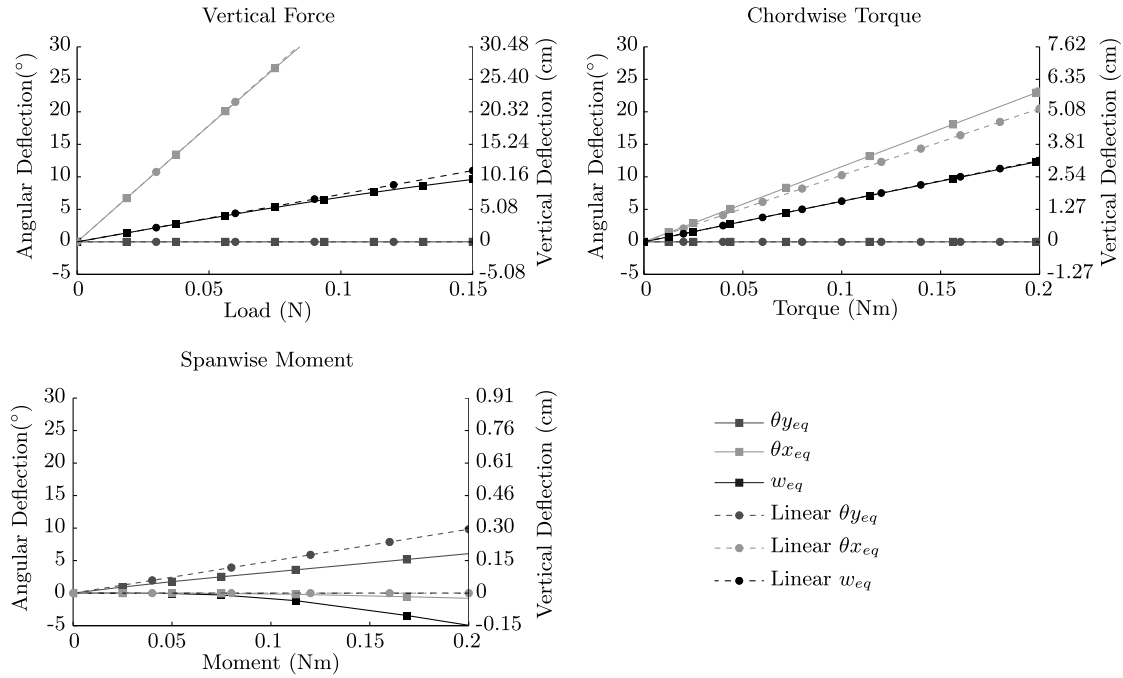| Load	x/c
5%	0.22850
10%	0.22851
15%	0.22854
25%	0.22879
50%	0.22962
75%	0.23182
100%	0.23558
Estimated value from Eq. (8)	0.22857

Fig. 3 Nonlinear results vs linear equivalent beam; vertical deflections, w_{eq}, are plotted against secondary y axis.
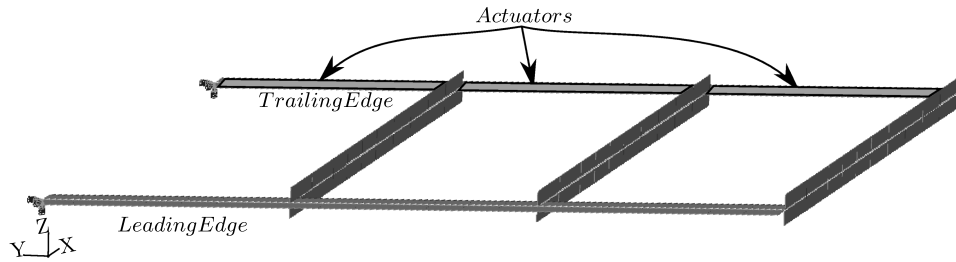

Fig. 4 Actuators applied to upper surface of trailing-edge spar.

equivalent-beam parameters of the options considered. The selected location is shown in Fig. 4.

V. Active Member

The manipulation of the location of the flexural axis, as well as other stiffness parameters, is accomplished by the implementation of a feedback loop relating the piezoelectric actuation to a displacement-based metric, such as strain. To examine the structural system, a model of the active member and feedback loop is first developed as an isolated cantilever beam with the piezoelectric actuator attached in a monomorph configuration.

There are generally two configurations for a beamlike piezoelec-tric actuator: monomorph and bimorph. In a monomorph configura-tion, a layer of piezoelectric material is attached to only one side of the substrate, whereas in a bimorph configuration piezoelectric layers are attached to the top and bottom of the substrate. In both configura-tions, a moment is induced via the piezoelectric effect by imparting an

internal stress/strain at some distance from the neutral axis of the assembly and is constant along the length of the actuator. A monomorph expands and contracts on one side of the substrate, whereas in a bimorph the two actuators work together, one extending while the other contracts. While a bimorph is more effective [24], a monomorph, as shown in Fig. 5, is used here for simplicity.

It is envisioned that macrofiber composite (MFC) actuators will be used in eventual implementation, and are used in the experimental validation of Sec. VI. MFC actuators were developed at NASA [25], and consist of piezoelectric material sliced into fibers of rectangular cross sections powered by interdigitated electrodes perpendicular to the fiber length [26]. It is known that MFC piezoelectric devices have a notable nonlinear nature culminating from various sources, none of which are accounted for in the presented analytical model; the impact of these linearized assumptions should be evaluated before imple-mentation on a per-design basis. A thorough theoretical discussion of piezoelectric hysteresis effects can be found in [27,28]. Piezoelectric and material nonlinearities specifically for the MFC actuators have
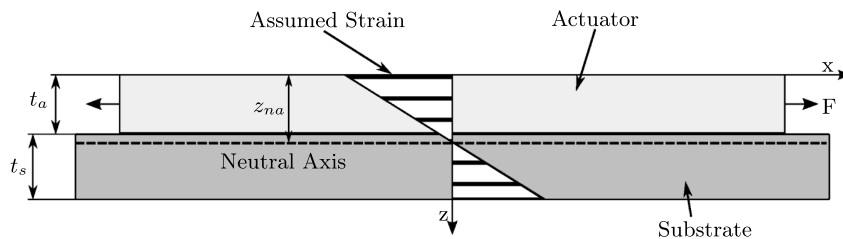

Fig. 5 Actuator diagram.

been experimentally investigated and documented by Williams [29] and Williams et al. [30,31]. The MFC actuators also have a nonuniform electrical field, which has been accurately modeled by Bilgen et al. [32].

For this analysis, a simple linear piezoelectric model will be used in conjunction with the Euler–Bernoulli beam theory, as discussed in Inman and Cudney [24]. The linear piezoelectric theory assumes monolithic piezoceramic material, in which the induced strain is linearly dependent on the elastic properties of the piezoceramic material and a uniformly applied electric potential field:

$$\sigma_k = C_{ki}^E(\epsilon_i - d_{ij}\Omega_j) \tag{13}$$

in which C_{ki}^E are the elastic stiffness constants obtained under constant electric field, ϵ_i are the deformation induced strains, $d_{ij}\Omega_j$ comprise the actuation induced strains, d_{ij} are the piezoelectric constants, and Ω_j is the applied electric field.

Using the modulus-weighted-section method, an equivalent width of the actuator is used in calculating the location of the neutral axis z_{na}. The dimensional quantities to be used later are $a1 = t_a + t_s - z_{na}$, $a2 = t_a - z_{na}$, and $a3 = -z_{na}$.

The total moment internal to the structure can be sorted into a moment internal to the active piezoelectric material M_a and a moment internal to the substrate material M_s. The active material moment M_a is found by integrating Eq. (13) through the thickness of the piezoceramic material, and multiplying terms by the appropriate width. The moment due to curvature κ stems from the strain term ϵ in Eq. (13), and is multiplied by the stiffness equivalent width of the actuator. The induced strain due to actuation Λ stems from the applied-electric-field terms Ω_i in Eq. (13), and is multiplied by the actual width of the actuator because the piezoelectric constants d_{ij} are determined for the isolated piezoelectric actuated beam:

$$M_a = \int_{a3}^{a2} \left(w_s \frac{E_a}{E_s} E_s \kappa z_{na}^2 - E_a w_a \Lambda z_{na} \right) dz \tag{14}$$

$$\mathbf{K}_a = \begin{pmatrix} \frac{12EI_{eq}}{L^3} & \frac{6EI_{eq}}{L^2} & -\frac{12EI_{eq}}{L^3} & \frac{6EI_{eq}}{L^2} \\ \frac{6[LEI_{eq}+Gn_a(L-2x_m)]}{L^3} & \frac{4Gn_aL+4LEI_{eq}-6Gn_ax_m}{L^2} & -\frac{6[LEI_{eq}+Gn_a(L-2x_m)]}{L^3} & \frac{2[LEI_{eq}+Gn_a(L-3x_m)]}{L^2} \\ -\frac{12EI_{eq}}{L^3} & -\frac{6EI_{eq}}{L^2} & \frac{12EI_{eq}}{L^3} & -\frac{6EI_{eq}}{L^2} \\ \frac{6(-Gn_aL+LEI_{eq}+2Gn_ax_m)}{L^3} & \frac{-4Gn_aL+2LEI_{eq}+6Gn_ax_m}{L^2} & \frac{6[-LEI_{eq}+Gn_a(L-2x_m)]}{L^3} & \frac{-2Gn_aL+4LEI_{eq}+6Gn_ax_m}{L^2} \end{pmatrix} \tag{20}$$

in which $\Lambda = (V_a/es)d_{33}$ determines the magnitude and direction of actuation, and es is the electrode spacing.

After evaluating the integral for the moment internal to the piezoelectric material, it can be separated into stiffness and actuation parts:

$$M_a = \frac{1}{3} E_a w_s (a2^3 - a3^3)\kappa + \frac{1}{2} E_a w_a(-a2^2 + a3^2)\Lambda$$
$$= E_a I_a \kappa + \frac{1}{2} E_a w_a(-a2^2 + a3^2)\frac{V_a}{es}d_{33} \tag{15}$$

in which I_a is the standard area moment of inertia evaluated relative to the neutral axis z_{na}.

By making the voltage proportional to the measured strain by a gain parameter, $V_a = Gn\epsilon = Gn\kappa(x_m)a1$, the actuation portion of Eq. (15) is made dependent on the curvature. For general loading configuration curvature, $\kappa(x_m)$ is not constant along the length of the beam, and in turn the measured strain is dependent on the location along the beam where the measurement is taken. To account for this, the curvature–displacement relationship of the Euler–Bernoulli beam

theory, $B(x)$, is used to calculate the curvature, and in turn strain, at a specified location:

$$B(x) = \left(-\frac{6}{L^2} + \frac{12x}{L^3}, -\frac{4}{L} + \frac{6x}{L^2}, \frac{6}{L^2} - \frac{12x}{L^3}, -\frac{2}{L} + \frac{6x}{L^2} \right) \tag{16}$$

After substituting and simplifying, the moment internal to the actuator becomes

$$M_a = E_a I_a \kappa + \frac{1}{2} E_a w_a(-a2^2 + a3^2)\frac{Gn}{es}d_{33}a1\kappa(x_m)$$
$$= E_a I_a \kappa + Gn_a B(x_m) \tag{17}$$

in which Gn_a is the additional gain-dependent term that effectively adds to the beam stiffness, and x_m is the location where the strain is measured.

Substituting the terms shown in Fig. 5 for the limits of integration, $a2$ and $a3$, Gn_a becomes

$$Gn_a = \frac{d_{33}E_aE_st_at_s(t_a+t_s)[E_st_s^2 + E_at_a(t_a + 2t_s)]w_a}{4es(E_at_a + E_st_s)^2}Gn \tag{18}$$

The moment internal to the substrate is found by integrating the internal stress through the thickness multiplied by the width of the substrate, resulting in the familiar $M_s = E_sI_s\kappa$.

Adding the internal moments of the actuator and the substrate, the governing bending equation of the combination becomes

$$M = M_s + M_a = \left(E_sI_s + E_aI_a \right)B(x) + Gn_aB(x_m)$$
$$= EI_{eq}B(x) + Gn_aB(x_m) \tag{19}$$

Premultiplying by the transpose of the curvature–displacement relationship, Eq. (16) results in an equivalent stiffness matrix for the beam-actuator feedback loop system:

VI. Experimental Validation

A. Test Rig

An experiment was conducted to validate the equivalent stiffness matrix of the beam-actuator feedback system shown in Eq. (20). As a cantilever beam is not a standard test configuration to determine material properties, a test rig had to be devised, as shown in Fig. 6. The rig is composed of an *XY* traverse, a load cell, and a large machinist right-angle bracket.

Two Velmex traverses with Anaheim Automation 23MDSI stepper motors were mounted together to form the *XY* traverse. The assembly was evaluated for accuracy and repeatability under load, and was found to be less than 1×10^{-5} m, which is the resolution of the digital calipers used for the evaluation. The load cell used is a JR3 model 30E12A4 with a range of ± 40 N, a resolution of 0.005 N in the axis used, and an accuracy of 0.25% of the measuring range for each axis, according to the company-published specifications. The load cell was mounted to the traverse with a small precision right-angle bracket. The test article was clamped to a large machinist precision right-angle block. The items comprising the test rig were arranged
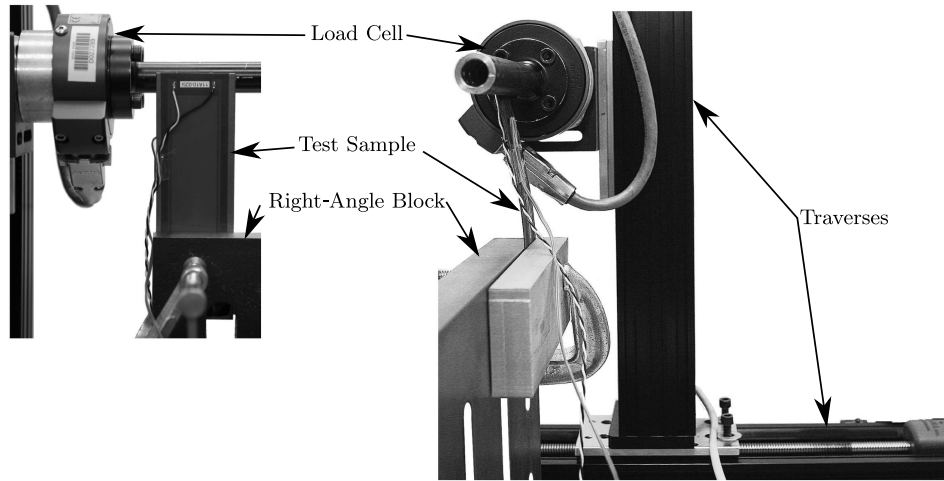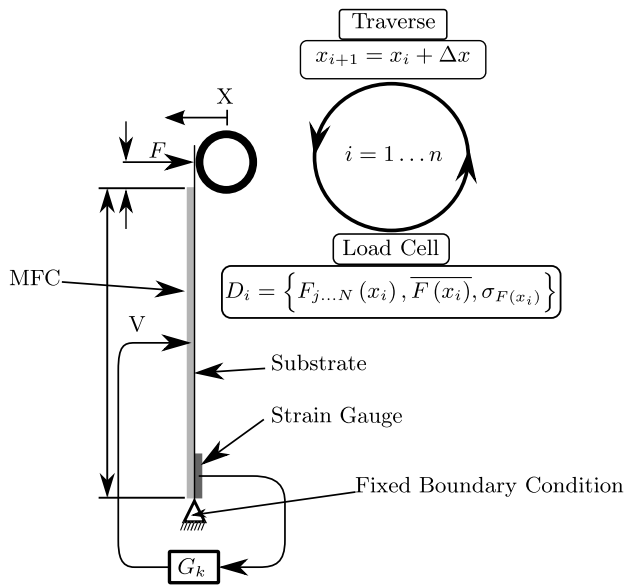
Fig. 6   Test rig.

Fig. 7   Experiment diagram.

on an optical table, aligned visually, and secured to maintain alignment.

The strain gauge adhered to the test sample was an Omega prewired, 10 mm long, 120 ohm resistance, with a 2.08 gauge factor. A National Instruments SCXI 1520 strain-gauge card with a SCXI 1314 connector box was used to read the strain gauge in a quarter-bridge configuration.

Actuation was achieved using an AM Power Systems AMD2012-CE3A dc–dc converter capable of transforming an input of 8–15 V to an output of -500 to $+1500$ V. This conversion is proportional to an input signal of 0–5 V controlling $\pm 100\%$ actuation, 2.5 V being zero actuation. The AM Power Systems circuit is designed specifically for driving MFC-type piezoelectric actuators.

For comparison to experimental data, a passive beam segment was added to the model using standard element assembly methods. By applying boundary conditions and conducting the appropriate manipulations, the applied tip force and displacement relationship is determined to be

$$F = \frac{6EI_{eq}E_sI_p(EI_{eq} + \mathrm{Gn}_a)}{2EI_{eq}D1 + \mathrm{Gn}_aD2}u$$

$$D1 = EI_{eq}L_p^3 + E_sI_pL_a(L_a^2 + 3L_aL_p + 3L_p^2)$$

$$D2 = 2EI_{eq}L_p^3 - E_sI_pL_a[L_a(L_a + 3L_p) - 3(L_a + 2L_p)x_m] \quad (21)$$

in which L_a is the actuator length, L_p is the length of the passive section at the beam tip Fig. 7, I_p is the area moment of inertia calculated about the neutral axis of the substrate, and u is the tip displacement.

A general uncertainty analysis, as described in [33], is conducted based on the force–displacement relation of Eq. (21), assuming 10% error in all material constants and ± 0.000005 m for all measured lengths; the resulting estimate and uncertainty for sample 1 are presented in Table 3.

B. Test Samples

Two sample configurations were tested: one steel substrate and one unidirectional carbon-fiber substrate. Each sample has a piezoelectric actuator model MFC 8528-P1 [26] attached to one side of the substrate, and a single strain gauge attached to the opposite side of the substrate toward what will be the base of the beam. Both sample configurations have the strain gauge mounted so that its lower edge is aligned with the lower edge of the active area of the MFC.

Steel was chosen as a substrate to minimize the unknown parameters for model verification. The steel substrates were cut from a 0.635-mm-thick sheet of low-carbon full-hard steel shim stock. The carbon-fiber substrate was cut from a previously cured sample of two layers of unidirectional carbon sandwiching a thin scrim layer of woven fiberglass with a total thickness of 0.33 mm.

C. Testing Procedure

The primary factor investigated in this experiment is the effect of the feedback loop, in which, in the MFC actuation, is proportional to the strain-gauge reading by a gain factor. During the course of each run, the feedback loop was run constantly, independent of the other test devices while readings were being taken. First, the traverse positioned the arm of the load cell a few millimeters from the test sample, and zero-load readings were recorded for the load cell and strain gauge. The traverse then translated the load cell by the determined distance in fixed increments, taking readings at each

Table 3   Sample 1 data

Test	Intercept	Standard error	Stiffness-gain slope	Standard error
1	1030.794	5.126	2.240e − 03	7.192e − 05
2	1035.630	3.758	2.249e − 03	5.272e − 05
3	1035.532	3.215	2.312e − 03	4.511e − 05
4	1060.356	5.253	2.121e − 03	7.370e − 05
5	988.781	3.775	2.240e − 03	5.296e − 05
6	974.832	2.748	2.286e − 03	1.512e − 04
Experimental mean	1020.987	13.216	2.241e − 03	2.684e − 05
Analytical prediction	1033.480	45.557	2.204e − 03	5.653e − 05

Table 4   Experiment design

Test	Sample	Total gain	Gain increments	Total deflection	Deflection increments	Load-cell samples	Hysteresis compensation
1	1	120,481	10	0.75	15	10,240	No
2	1	120,481	10	0.75	15	10,240	No
3	1	120,481	10	0.75	15	10,240	No
4	1	120,481	10	0.75	15	2,048	No
5	1	120,481	10	0.75	15	2,048	Yes
6	1	30,000	5	0.50	20	2,048	Yes
7	2	82,907	10	2.00	20	2,048	No
8	2	82,907	10	2.00	20	2,048	Yes
9	2	82,907	20	2.00	20	2,048	Yes
10	2	82,907	10	2.00	20	2,048	Yes
11	2	16,581	10	1.50	15	2,048	Yes
12	2	82,907	5	1.00	20	2,048	Yes

increment. All of the measurement data were recorded, as well as the mean and standard deviation at each increment. After each displacement cycle, the gain factor was incrementally increased, and the displacement/measurement cycle was started again.

As discussed in Sec. V, the hysteresis effects are a significant concern for piezoelectric devices. To investigate the influence of hysteresis from run to run, a wiping cycle was conducted before each deflection sequence for some of the tests. This wiping cycle consisted of electrically actuating the sample to the maximum limit, minimum limit, and then returning it to zero. This ensures the sample is returned to the same point in the hysteresis loop before the start of the next testing sequence, eliminating the memory aspects of hysteresis.

The total displacement for each sample was determined by advancing the load cell by set increments until a specified force was reached: 7.00 N for sample 1, and 1.70 N for sample 2. The values of these forces were selected to provide an adequate range of force and displacement to enable discernment given the accuracy of the instrumentation and traverse. The strain measurement at the determined maximum deflection for each sample was noted, ϵ_d. The values of ϵ_d were then used to determine the maximum gain value. Assuming the given deflection will result in approximately the same strain measurement under actuation, the total gain is calculated as $Gn_t = sf 1500/\epsilon_d$ with a safety factor of 0.9. These values describing the parameters and sample for each run are presented in Table 4; a sample rate of 2048 was used for the load cell for all of the tests.

Electric field Ω is a function of the applied voltage, and depends on the geometry and spacing of the electrodes. From linear piezoelectric theory, $\Omega = V_a/es$, in which es = 0.5 mm is the electrode spacing for MFC piezoelectric actuators, and V_a is the applied voltage. Electrical limits of $+1500$ to -500 V are imposed on the MFC actuators due to failure in the form of dielectric breakdown, making the limits on the electrical field 3000 V/mm $< \Omega < -1000$ V/mm. These limits must be taken into account when selecting a range of possible values for the gain parameter Gn so as to avoid overloading and failure in the form of dielectric breakdown. During the course of the testing, the electric field was limited to 90% of the maximum and minimum limits for safety purposes.

D. Postprocessing and Error Analysis

At the beginning of each displacement cycle, voltage values for the unloaded configuration are taken from the load cell. The mean of these no load voltages is subtracted from the subsequent measurement, accounting for any zero offset in the instrument, as well as taring the weight of the arm. Next, with the tare taken out, the voltages are multiplied through a calibration matrix provided by the manufacturer, relating the measured voltages to a corresponding force. The calculated forces are then used to determine the effective bending stiffness of the beam for each gain value. Then, the relation of the values for bending stiffness to the gain parameter is determined.

A linear least-squares estimation is used to postprocess the results of the test runs. The MATLAB Statistics Toolbox is primarily used, specifically the least-squares robust fit function using the default "bisquare" weight function. The least-squares robust function recursively evaluates each data point and automatically determines if it is suspect as an outlier by assigning a weight value to it. A weighting value of zero indicates that particular data point is not reliable, should be suspected as an outlier and subsequently removed. To determine an estimate for the uncertainty in the slope and intercept, standard uncertainty expressions are used [33]. The random uncertainty terms are found from the variance of the data, and systematic uncertainty terms are taken as load-cell accuracy $[(0.1 \text{ N})^2]$ and traverse accuracy $[(1 \times 10^{-5} \text{ m})^2]$.

For the first phase of postprocessing, the parameter of interest is stiffness, the slope term of the assumed linear relation between force and displacement. For purposes of model validation, we focus on test sample 1. A plot of the collected force–displacement data from test 4, corrected to a zero intercept, is presented in Fig. 8 with linear least-squares results and standard-deviation error bars. The test 4 data set is representative of the data sets collected with sample 1. As can be observed from the data, the gain parameter has a statistically significant influence on the force — displacement relation.

Using the slope values, associated uncertainty terms, and corresponding gain values, a second linear least-squares regression is conducted on the data to determine the stiffness-gain relations. The uncertainty calculated for the force-displacement slope is taken as the systematic uncertainties in the secondary slope-and-intercept calculations. The intercept of the stiffness-gain relation is the passive stiffness of the composite beam. The determined stiffness-gain relations, with 95% confidence intervals, for all of the tests conducted with sample 1, are presented in Fig. 9 along with the analytical model and standard error. The confidence intervals are calculated using the standard deviation, t-distribution, and the number of gain increments for the test. The slope-and-intercept parameters from the regression analysis and analytical model are presented in Table 3 with corresponding standard errors. The six experimental data sets presented are identified as tests 1–6 in Table 4, with the raw data, linear fit, and confidence intervals for each.
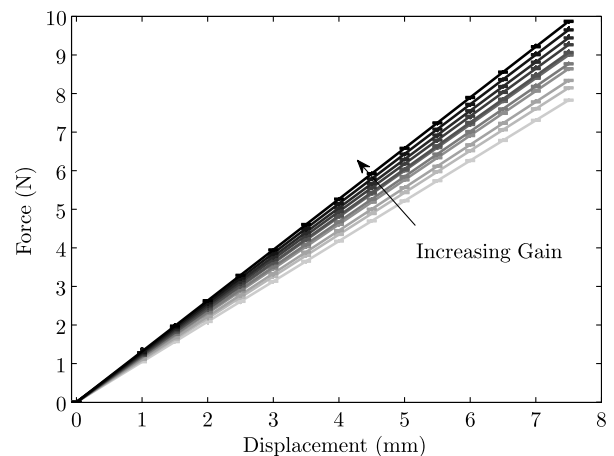
Fig. 8   Force-displacement relationship for sample 1, test 4.
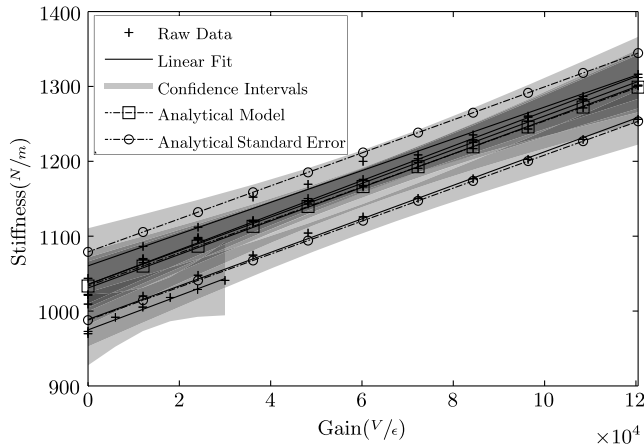
Fig. 9 Stiffness-gain relationship for sample 1: experimental data and analytical prediction.
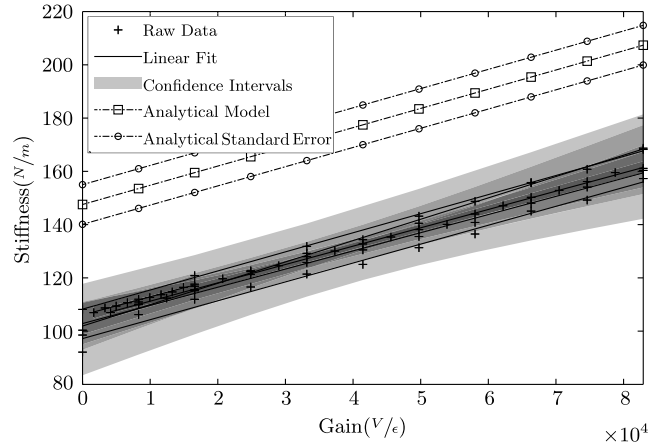
Fig. 10 Stiffness-gain relationship for sample 2: experimental data and analytical prediction.

The standard-error calculations for the analytical model are based on assuming 5% uncertainty in material properties and $(1 \times 10^{-5} \text{ m})^2$ uncertainty in all length measurements. The overlap of the confidence intervals illustrates the repeatability of the tests and the statistical insignificance of the hysteresis compensation in tests 5 and 6. Over the range tested, the analytical model shows excellent agreement with the experiment data; the results are presented in Table 3 and in Fig. 9.

The carbon-fiber-substrate sample is more representative of the envisioned design than the steel. The experimental results for sample 2, presented in Fig. 10, show 50% increase in the stiffness of the configuration tested. The dramatic results from this unoptimized design, with a limited actuation range, speak to the feasibility of the FACt adaptive aerostructure concept.

The analytical-experimental discrepancy for the carbon-fiber sample is more significant than the steel. The intercept error can be attributed to the isotropic material assumptions in the analytical model, which can be addressed by using a laminated-plate theory to more properly integrate material properties and ply orientations through the thickness of the substrate.

Hysteresis is commonly the first suspect for nonlinearities in piezoelectric devices. If hysteresis was to be a concern with this system, one would expect the effect to be more prominent with the carbon-fiber substrate than with the steel-based samples. Because of the higher bending stiffness, the steel sample would have a greater ability to overcome any residual stresses/strains in the piezoelectric material. The hysteresis compensation step was added to the test procedure to investigate this possibility.

Although an inadequate number of tests were conducted to make a conclusive statement (see Table 4), the hysteresis compensation made no discernible difference to the carbon-fiber results, as presented in Table 5. This suggests the nonlinearity, if present at all, in an actuator system of this configuration, is likely a dependency on applied stress, as discussed by Williams et al. [30], and not due to piezoelectric hysteresis.

Hysteresis in piezoelectric devices is due to residual stresses/strains in the piezoelectric material after actuation or deflection [27]. These residuals effect the nonactuated/nonloaded configuration, which is typically considered to be a reference point in actuation system design or control. The design paradigm implemented here inherently excludes the need for such a reference point. By focusing on changing the stiffness as a metric instead of changing the geometry, the consistent force-producing capability of the piezoelectric actuators is used instead of the problematic deflecting capability. Another perspective is that the feedback loop, attempting to return the system to a zero deflection, is inherently compensating for residual hysteretic strains.

VII. Active Structure

Incorporating the active stiffness matrix $\mathbf{K}_a(\text{Gn})$, Eq. (20), into the analysis of Sec. III as the stiffness matrix of the trailing-edge spar, element 3, an active version of the reduced compliance matrix, Eq. (5), is found, $\mathbf{C}_{\text{red}} \Rightarrow \mathbf{C}_a(\text{Gn})$. This active compliance matrix is then used in the same way as the passive variant to find the location of the active flexural axis:

$$ax_{\text{fa}} = \frac{x}{c} = \frac{L\{EI_3(EI_3 + \text{Gn}_a)Ls_2 + EI_1[4EI_3^2 + EI_3(4\text{Gn}_a + Ls_2) + 3\text{Gn}_a s_2 (L - 2x_m)]\}}{4EI_1 EI_3(EI_t + \text{Gn}_a)L + EI_t(EI_t + \text{Gn}_a)L^2 s_2 - 2EI_1^2 \text{Gn}_a(L - 3x_m)} \tag{22}$$

in which $EI_t = (EI_1 + EI_3)$, and the gain-dependent piezoelectric actuation term Gn_a is defined in Eq. (18). It is noted that, when $\text{Gn}_a = 0$, Eq. (8) is recovered.

With EI_3 defined and using Eq. (9) so that $EI_1 = EI_3[(1/x_{\text{fa}}) - 1]$, the location of the active axis is found as a function of the passive axis location. Subtracting the passive axis location from this gives the increment of axis relocation in terms of the experimentally determined factors, in which EI_3 is the intercept and Gn_a is the slope:

$$ax_{\text{fa}} - x_{\text{fa}} = \frac{3\text{Gn}_a(x_{\text{fa}} - 1)x_{\text{fa}}[-Ls_2(L - 2x_m) + 2EI_3(x_{\text{fa}} - 1)(L - x_m)]}{L\{-4EI_3^2(x_{\text{fa}} - 1) + \text{Gn}_a Ls_2 x_{fa} + EI_3[Ls_2 + \text{Gn}_a(-2 + 8x_{\text{fa}} - 6x_{\text{fa}}^2)]\} + 6EI_3 \text{Gn}_a(x_{\text{fa}} - 1)^2 x_m} \tag{23}$$

The preceding equation reveals the relevant parameters and their relationships, providing critical insight into the design. This equation would serve as a centerpiece for a design and optimization framework.

Substituting the mean values for the carbon-fiber sample from Table 5 results in

$$ax_{\text{fa}} - x_{\text{fa}} = \frac{0.0021849 Gn(x_{\text{fa}} - 1)x_{\text{fa}}(-18.6355 + 18.6319x_{\text{fa}})}{4065.7 - 4065.28x_{\text{fa}} + Gn[-0.012064 + (0.0527757 - 0.0407087x_{\text{fa}})x_{\text{fa}}]} \tag{24}$$

Table 5 Sample 2 data

Test	Intercept	Standard error	Stiffness–gain slope	Standard error
7	97.672	1.532	6.975e − 04	3.124e − 05
8	102.481	1.087	7.795e − 04	2.215e − 05
9	103.698	0.414	7.013e − 04	8.541e − 06
10	102.392	0.743	6.896e − 04	1.514e − 05
11	105.491	0.596	7.782e − 04	6.078e − 05
12	108.431	0.600	7.235e − 04	1.195e − 05
Experimental mean	103.361	1.465	7.283e − 04	1.665e − 05
Analytical prediction	147.557	7.450	7.215e − 04	3.861e − 05

Table 6 Values of structural parameters for active analysis

	Length, m	Height, m	Width, m	EI_i, N · m²	s_i, N · m
Leading-edge spar	0.095	5.974E − 4	0.04	0.105	1.684
Trailing-edge spar	0.095	6.600E − 4	0.04	0.029	0.480
Rib	0.152	0.0127	6.600E − 4	16.674	0.450

Table 7 Values of structural parameters for active analysis (continued)

Parameter	Values
E	148 GPa
E_a	29.4 GPa
x_{fa}	0.22
d_{33}	460E − 12 (m/V)
w_a	0.04 m
t_a	3.0E − 3 m
x_m	0.005
X	0.25c
Lf	5 N
Rt	0.33 N · m
Mo	0.68 N · m

Using this implemented configuration as an unoptimized baseline a results in a possible flexural-axis relocation of ~22% with a passive axis location of 39% at gain of 100,000. A possible configuration of interest for a detailed design study is to make the structural chord a subset of the aerodynamic chord. This would allow more freedom in the design. Any advantages/disadvantages would have to be evaluated in an absolute scale.

Using the location of the active flexural axis ax_{fa} and the active compliance matrix $C_a(Gn)$, an active version of the equivalent-beam compliance matrix in Eq. (12) can be derived:

$$\begin{pmatrix} w_{eq} \\ \theta x_{eq} \\ \theta y_{eq} \end{pmatrix} = \begin{pmatrix} (1 - ax_{fa}) & 0 & 0 & ax_{fa} & 0 \\ 0 & 0 & (1 - ax_{fa}) & 0 & ax_{fa} \\ 0 & 1 & 0 & 0 & 0 \end{pmatrix}$$
$$\cdot \, C_a(Gn) \cdot [F(ax_{fa}c) + T(ax_{fa}c) + M(ax_{fa}c)] \tag{25}$$

Just as in Sec. III, the equivalent-single-beam compliance matrix Ca_{eq} is found by factoring out the point loads Lf, Rt, and Mo:
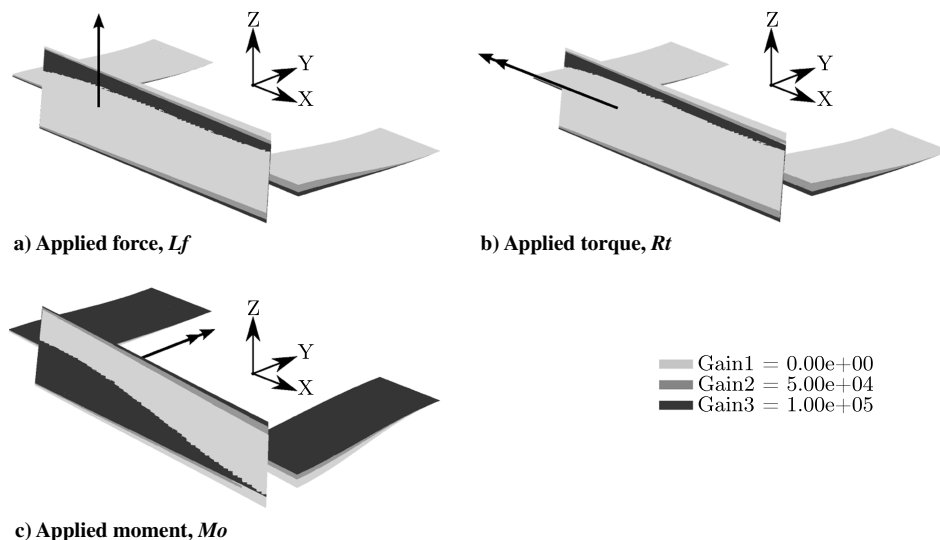
$$\begin{pmatrix} w_{eq} \\ \theta x_{eq} \\ \theta y_{eq} \end{pmatrix} = Ca_{eq}(Gn) \begin{pmatrix} Lf \\ Rt \\ Mo \end{pmatrix} \tag{26}$$

The active version of the equivalent compliance matrix has the same form as the passive, but is too large to be presented here. This derivation shows that the proposed structural configuration and actuation system will enable the control of the three structural parameters: the location of the flexural axis, bending stiffness, and twisting stiffness.

The active reduced compliance matrix $C_a(Gn)$, the mathematical model for the representative subsection presented in Fig. 1b, was implemented numerically. An analysis was conducted using the parameter values presented in Tables 6 and 7. The height, or thickness, of the trailing-edge spar includes both the thickness of the actuator and the thickness of the structural member. The structural system was evaluated with a constant point load, moment, and torque applied at 25% of the chord and various values for the gain. The range of gain values was determined by dividing the upper limit of Ω by the calculated strain from the applied vertical force with the structure in the passive state. The resulting deformation of the representative subsection is presented in Fig. 11.

From the figures, it can be seen that increasing the gain parameter results in a reversal of the structural response. This phenomenon can be explained in the context of the preceding analysis as the result of moving the flexural axis. When the axis is moved to the other side of the applied force, the rotational deformation naturally changes direction.

Conceptually, this change in structural response can be used as a control effector. With an increase in the gain, the axis moves aft, which will effectively stiffen the flexible structure, making the vehicle more responsive. And if the axis is moved far enough, actuation can put the wing in an aeroelastically divergent configuration, whereby the wing flares to higher twist angles proportionally to the wing loading and gain value. The commanded and controlled divergence, in turn, would generate a significant change in force distribution, effectively using the entire wing as a control surface.

a) Applied force, *Lf*

b) Applied torque, *Rt*

c) Applied moment, *Mo*

Gain1 = 0.00e+00
Gain2 = 5.00e+04
Gain3 = 1.00e+05

Fig. 11 Structural system response to applied static point with indicated gain values; deformations are not magnified.

VIII. Conclusions

A structural system design, with the potential to simultaneously enhance the disturbance rejection and maneuvering performance of an aerial vehicle, was presented. The enhancements are achieved through aeroelastic interactions enabled by actively controlling the location of the wing's flexural axis in flight. The FACt system functions by changing the stiffness of the rear spar of a standard wing structure through incorporation of an embedded actuator acting in conjunction with a displacement sensor in a simple feedback loop. The spar's effective stiffness is controlled of by the gain parameter of the feedback loop.

Although linear theories were primarily used in the formulation, the results were shown to be satisfactorily consistent in the nonlinear regime. A bend–twist coupling, resulting from geometrical non-linearities, is not captured by the linear formulation; the magnitude of the coupling will be dependent on the design details of the vehicle to which the system is applied. An experiment was conducted validating the derived actuation model. The potential and feasibility of the FACt system were analytically demonstrated with an unoptimized configuration, wherein the flexural axis was relocated by approximately 22%.

Future research will include a quantitative analysis investigating the relations between the structural parameters of a wing, their magnitude/location and rate of change, and the flight mechanics/dynamics of the vehicle in an effort to assess unanticipated or nonintuitive results from application of concepts, such as that presented in this paper.

References

[1] Ifju, P. G., Ettinger, S., Jenkins, D., and Martinez, L., "Composite Materials for Micro Air Vehicles," *SAMPE Journal*, Vol. 37, May 2001, pp. 7–12.

[2] Ifju, P. G., Jenkins, D. A., Ettinger, S., Lian, Y., Shyy, W., and Waszak, M. R., "Flexible-Wing-Based Micro Air Vehicles," AIAA Paper 2002-0705, 2002.
doi:10.2514/6.2002-705

[3] Livne, E., "Future of Airplane Aeroelasticity," *Journal of Aircraft*, Vol. 40, No. 6, 2003, pp. 1066–1092.
doi:10.2514/2.7218

[4] Kota, S., Hetrick, J., and Saggere, L., "Design of a Variable Stiffness Spar," CSA Engineering, ASIAC-TR-97-01, Palo Alto, CA, Jan. 1997.

[5] Chen, P. C., Sarhaddi, D., Jha, R., Liu, D. D., Griffin, K., and Yurkovich, R., "Variable Stiffness Spar Approach for Aircraft Maneuver Enhancement Using ASTROS," *Journal of Aircraft*, Vol. 37, No. 5, 2000, pp. 865–871.
doi:10.2514/2.2682

[6] Amprikidis, M., and Cooper, J., "Development of Smart Spars for Active Aeroelastic Structures," *44th AIAA/ASME/ASCE/AHS/ASC Structures, Structural Dynamics, and Materials Conference*, AIAA, Reston, VA, 2003, pp. 1–11.
doi:10.2514/6.2003-1799

[7] Cooper, J., "Adaptive Stiffness Structures for Air Vehicle Drag Reduction," *Multifunctional Structures/Integration of Sensors and Antennas*, NATO Science and Technology Organization, Neuilly-sur-Seine, France, 2006, pp. 15-1–15-12; also NATO RTO-AVT-141, 2006.

[8] Barbarino, S., Bilgen, O., Ajaj, R. M., Friswell, M. I., and Inman, D. J., "A Review of Morphing Aircraft," *Journal of Intelligent Material Systems and Structures*, Vol. 22, No. 9, 2011, pp. 823–877.
doi:10.1177/1045389X11414084

[9] Bisplinghoff, R., Ashley, H., and Halfman, R., *Aeroelasticity*, Dover, New York, 1996, pp. 800–810.

[10] Dowell, E., et al., *A Modern Course in Aeroelasticity*, 4th ed., Kluwer Academic, Norwell, MA, 2004, pp. 20–50.

[11] Rodden, W., *Theoretical and Computational Aeroelasticity*, Crest Publishing, Burbank, CA, 2011, pp. 10–20.

[12] Cook, R., *Concepts and Applications of Finite Element Analysis*, 4th ed., Wiley, New York, NY, 2002, pp. 20–50.

[13] Barrett, R., "Active Aeroelastic Tailoring of an Adaptive Flexspar Stabilator," *Smart Materials and Structures*, Vol. 5, No. 6, 1996, pp. 723–730.
doi:10.1088/0964-1726/5/6/001

[14] Barrett, R., "All-Moving Active Aerodynamic Surface Research," *Smart Materials and Structures*, Vol. 4, No. 2, 1995, pp. 65–74.
doi:10.1088/0964-1726/4/2/001

[15] Barrett, R., "Aeroservoelastic DAP Missile Fin Development," *Smart Materials and Structures*, Vol. 2, No. 2, 1993, pp. 55–65.
doi:10.1088/0964-1726/2/2/001

[16] Bilgen, O., "Macro Fiber Composite Actuated Unmanned Air Vehicles: Design, Development, and Testing," M.S. Thesis, Dept. of Mechanical Engineering, Virginia Polytechnic Institute and State Univ., Blacksburg, VA, 2007.

[17] Bilgen, O., Ohanian, O., III, Kochersberger, K., and Inman, D., "Novel, Bidirectional, Variable-Camber Airfoil via Macro-Fiber Composite Actuators," *Journal of Aircraft*, Vol. 47, No. 1, 2010, pp. 303–314.
doi:10.2514/1.45452

[18] Bilgen, O., Kochersberger, K., Inman, D., and Ohanian, O., III, "Macro-Fiber Composite Actuated Simply Supported Thin Airfoils," *Smart Materials and Structures*, Vol. 19, No. 5, 2010, Paper 055010.
doi:10.1088/0964-1726/19/5/055010

[19] Ohanian, O., III, Karni, E., Olien, C., Gustafson, E., Kochersberger, K., Gelhausen, P., and Brown, B., "Piezoelectric Composite Morphing Control Surfaces for Unmanned Aerial Vehicles," *Proceedings of the SPIE Conference on Sensors and Smart Structures Technologies for Civil, Mechanical, and Aerospace Systems*, Vol. 7981, Soc. of Photo-Optical Instrumentation Engineers, Bellingham, WA, 2011, pp. 1–13.
doi:10.1117/12.881770

[20] Ehlers, S., and Weisshaar, T., "Adaptive Wing Flexural Axis Control," *3rd International Conference on Adaptive Structures*, Technomic, Lancaster, PA, 1993, pp. 28–40.

[21] Ehlers, S., and Weisshaar, T., "Effect of Adaptive Material Properties on Static Aeroelastic Control," *33rd Structures, Structural Dynamics, and Materials Conference*, AIAA, Washington, DC, 1992, pp. 914–924.
doi:10.2514/6.1992-2526.

[22] Weisshaar, T., "Static Aeroelastic Behavior of an Adaptive Laminated Piezoelectric Composite Wing," *31st Structures, Structural Dynamics, and Materials Conference*, AIAA, Washington, DC, 1990, pp. 1611–1623.
doi:10.2514/6.1990-1078

[23] Weisshaar, T. A., and Ehlers, S. M., "Adaptive Aeroelastic Composite Wings—Control and Optimization Issues," *Composites Engineering*, Vol. 2, Nos. 5–7, 1992, pp. 457–476.
doi:10.1016/0961-9526(92)90037-7

[24] Inman, D., and Cudney, H., "Structural and Machine Design Using Piezoceramic Materials: A Guide for Structural Design Engineers," NASA TR NAG1-1998, 2000.

[25] Wilkie, W. K., Bryant, R. G., High, J. W., Fox, R. L., Hellbaum, R. F., Jalink, J. A., Little, B. D., and Mirick, P. H., "Low-Cost Piezocomposite Actuator for Structural Control Applications," *Proceedings of the SPIE Smart Structures and Materials 2000: Industrial and Commercial Applications of Smart Structures Technologies*, edited by Jacobs, J. H., Vol. 3991, Soc. of Photo-Optical Instrumentation Engineers, Bellingham WA, 2000, pp. 323–334.

[26] "Macro Fiber Composite (MFC) Brochure," Smart Material Corp., Sarasota, FL, http://www.smart-material.com [retrieved 13 April 2013].

[27] Bertotti, G., and Mayergoyz, I., "Hysteresis in Materials," *The Science of Hysteresis*, Vol. 3, Academic Press, London, 2006, pp. 337–465.

[28] Bilgen, O., Friswell, M., and Inman, D., "Theoretical and Experimental Analysis of Hysteresis in Piezocomposite Airfoils Using Preisach Model," *Journal of Aircraft*, Vol. 48, No. 6, 2011, pp. 1935–1947.
doi:10.2514/1.C031374

[29] Williams, R. B., "Nonlinear Mechanical and Actuation Characterization of Piezoceramic Fiber Composites," Ph.D. Dissertation, Dept. of Mechanical Engineering, Virginia Polytechnic Institute and State Univ., Blacksburg, VA, 2004.

[30] Williams, R., Inman, D., and Wilkie, W., "Nonlinear Response of the Macro Fiber Composite Actuator to Monotonically Increasing Excitation Voltage," *Journal of Intelligent Material Systems and Structures*, Vol. 17, No. 7, 2004, p. 601–608.

[31] Williams, R. B., Inman, D. J., Schultz, M. R., Hyer, M. W., and Wilkie, W. K., "Nonlinear Tensile and Shear Behavior of Macro Fiber Composite Actuators," *Journal of Composite Materials*, Vol. 38, No. 10, 2004, pp. 855–869.
doi:10.1177/0021998304040555

[32] Bilgen, O., Erturk, A., and Inman, D. J., "Analytical and Experimental Characterization of Macro-Fiber Composite Actuated Thin Clamped-Free Unimorph Benders," *Journal of Vibration and Acoustics*, Vol. 132, No. 5, 2010, Paper 051005.
doi:10.1115/1.4001504

[33] Coleman, H. W., and Steele, W. G., *Experimentation and Uncertainty Analysis for Engineers*, 2nd ed., Wiley-Interscience, New York, 1998, pp. 208–215.